

Exploring deep defect state impact on open circuit voltage of conventional and inverted organic solar cells

Aniket Rana,^{1,2,a)} Amit Kumar,^{1,2} Suresh Chand,^{1,2} and Rajiv K. Singh^{1,2,a)}

¹CSIR- National Physical Laboratory, Dr. K. S. Krishnan Marg, New Delhi 110012, India

²Academy of Scientific and Innovative Research (AcSIR), CSIR-NPL Campus, New Delhi 110012, India

(Received 16 June 2018; accepted 21 August 2018; published online 11 September 2018)

In this manuscript, conventional and inverted organic solar cells based on P3HT:PC[60]BM have been explored to understand the effect of deep defect states on the open circuit voltage. The enhancement in the open circuit voltage in the inverted structure compared to the conventional structure has been comprehensively discussed in terms of density of defect states. To comply with the investigation, DC and AC measurements (impedance spectroscopy) at various temperatures have been performed extensively. Enhancement in open circuit voltage at low temperature is observed which is described by the shifting of hole and electron quasi-Fermi levels. The important observation from the defect density of states profile is that the center of Gaussian distribution is shifted to high energy as the temperature is increased which is an indication of the creation of shallow traps in polymers. In the inverted device, the disorder parameter (σ) is 33 meV, whereas in the conventional device it becomes 75 meV. This implies that the energetic disorder is reduced in an inverted device which helps in the improvement of open circuit voltage. *Published by AIP Publishing.* <https://doi.org/10.1063/1.5045099>

INTRODUCTION

In the organic solar cell, the donor-acceptor system is utilized to break the exciton¹ to separate the free carriers. The donor-acceptor material blend also provides a large interface area for exciton breaking.² The performance of organic solar cells primarily depends on the localized states within the bandgap of polymers. It is well established that by increasing the density of states, the electronic parameters of solar cells can be improved.³ Recombination of electrons in the acceptor lowest unoccupied molecular level (LUMO) to the holes in the donor highest occupied molecular level (HOMO) is a critical factor for the device performance limitation. There are numerous types of recombination processes in organic solar cells which exhibit different kinetic properties depending on the material and device structure. The bimolecular and Shockley Read Hall (SRH) (trap-assisted) recombination (monomolecular) process is most relevant in the organic solar cells.^{4–6} In the bimolecular recombination process, the electron and hole originated from different excitons recombine, whereas in the SRH free charge recombines with another charge at the interfacial trap state. The impurities in the donor acceptor materials and incomplete phase separation are likely to contribute in SRH recombination. These recombination processes have vital impact on the open circuit voltage of organic solar cells.⁷ Usually the bimolecular recombination is known to be dominant at the open circuit voltage condition and if the traps are available in the device, the open circuit voltage is adversely affected.⁸ Commonly the open circuit voltage is calculated from the difference of the LUMO and HOMO^{9,10} of the acceptor and donor consequently. Scharber *et al.*¹¹ have studied open circuit voltage for the wide range of

material combinations, and they found the empirical relationship, $eV_{oc} = E_g - 0.3 \text{ eV}$ where E_g is the donor-acceptor bandgap. Later this study was proved invaluable for a new generation of donor polymers⁹ because it provides little information about the physical origin of open circuit voltage. From the current-voltage characteristics of the solar cell, open circuit voltage denotes the potential at which the total output voltage becomes zero that fundamentally means the balance between the charge carrier generation and recombination in the solar cell. Numerous studies have found the strong relation between the charge transfer (CT) state and open circuit voltage. This type of study raises the question of the dependence of the open circuit voltage on the donor-acceptor energy gap is causal or just accidental. By the principle of detailed balance, it was argued that the CT state would influence the open circuit voltage only when the radiative CT state is the limiting loss mechanism.¹² It was also discussed that the reduction in the CT state emission might enhance the device performance with the uncertainties like the effect of non-radiative losses.¹³ A detailed study of electronic defect state distribution in the donor-acceptor blend, in connection with the open circuit voltage, is required to explore the opportunity for improvement in the device performance.¹⁴ Commonly defect states introduce recombination centers leading to a loss of free carriers.¹⁵ In the literature, it is found that the inverted structure shows higher circuit voltage compared to the conventional structure. In particular, the reduced series resistance in the inverted type organic solar cell produces less series resistance compared to the conventional organic solar cell. It is caused by the reduced recombination at the interface thereby producing higher open circuit voltage.¹⁶ Here, the reason for enhancement in open circuit voltage has been explored through the study of deep defect state distribution in the inverted as well as conventional devices.^{17,18} The exploration of this fundamental aspect starts

^{a)}Electronic addresses: aniket.rana@gmail.com and rajivsingh@nplindia.org

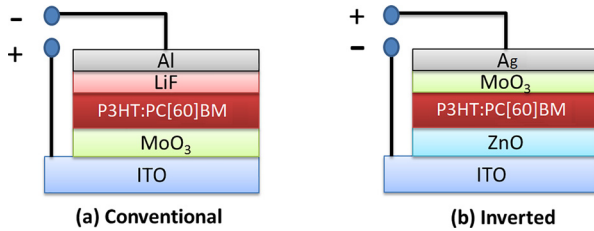


FIG. 1. Structure of the (a) conventional organic solar cell (ITO/Mo₃/P3HT:PC[60]BM/LiF/Al) and (b) inverted organic solar cell (ITO/ZnO/P3HT:PC[60]BM/Mo₃/Ag).

from the study of current-voltage characteristics of the conventional and inverted device based on the P3HT:PC[60]BM blend. The steeper distribution of defect states at low temperature also describes the open circuit voltage increment.

EXPERIMENTAL METHOD

Organic solar cells have been fabricated with two structures viz. conventional and inverted. The conventional device structure is ITO/Mo₃/P3HT: PC[60]BM/LiF/Al whereas the inverted device structure is ITO/ZnO/P3HT:PC[60]BM/Mo₃/Ag. The blending ratio of the P3HT:PC[60]BM blend was 1:0.8 by weight with 30 mg ml⁻¹ solution concentration in dichlorobenzene. An indium tin oxide (ITO) coated glass

substrate was patterned with a laser scriber and then ultrasonicated in a soap solution, acetone, and then isopropyl alcohol stepwise each for 20 min. After that, it was UV-Ozone treated for 7 min. Mo₃ (8 nm) and LiF (1 nm) were used as a buffer layer, deposited by the vacuum deposition process. The preparation of the zinc oxide (ZnO) electron transport layer for the inverted solar cell starts with following the initial steps. In a vial, 137.6 mg zinc acetate (ZnAc) added to 45.35 μ l of the Ethanolamine and 1 ml of 2-methoxyethanol were taken. a stir bar was dropped and closed and then was put it on a stir plate for at least 1 h at 60 °C. To deposit, first pre-cleaned ITO was taken and then 0.2 ml of ZnO solution was dropped on the substrate and spin cast at 3000 rpm for the 60 s. A Q-tip wetted with acetonitrile was used to wipe off the ITO contact pads (it removes the ZnO over the ITO to get a better contact). Next, the substrate was annealed at 300 °C for 10 min. The active layer (P3HT: PC[60]BM (1:1)) film was spin coated at 800 rpm for 60 s and annealed at 120 °C for 20 min. Aluminium (Al) and silver (Ag) used as an electrode was thermally evaporated up to 100 nm over the active layer at 10⁻⁶ mbar pressure with around 2 Å per second deposition rate. The final achieved cell structure is ITO/Mo₃/P3HT:PC[60]BM/LiF/Al with an area of 0.09 cm². The J-V characterization was performed under darkness as well as at

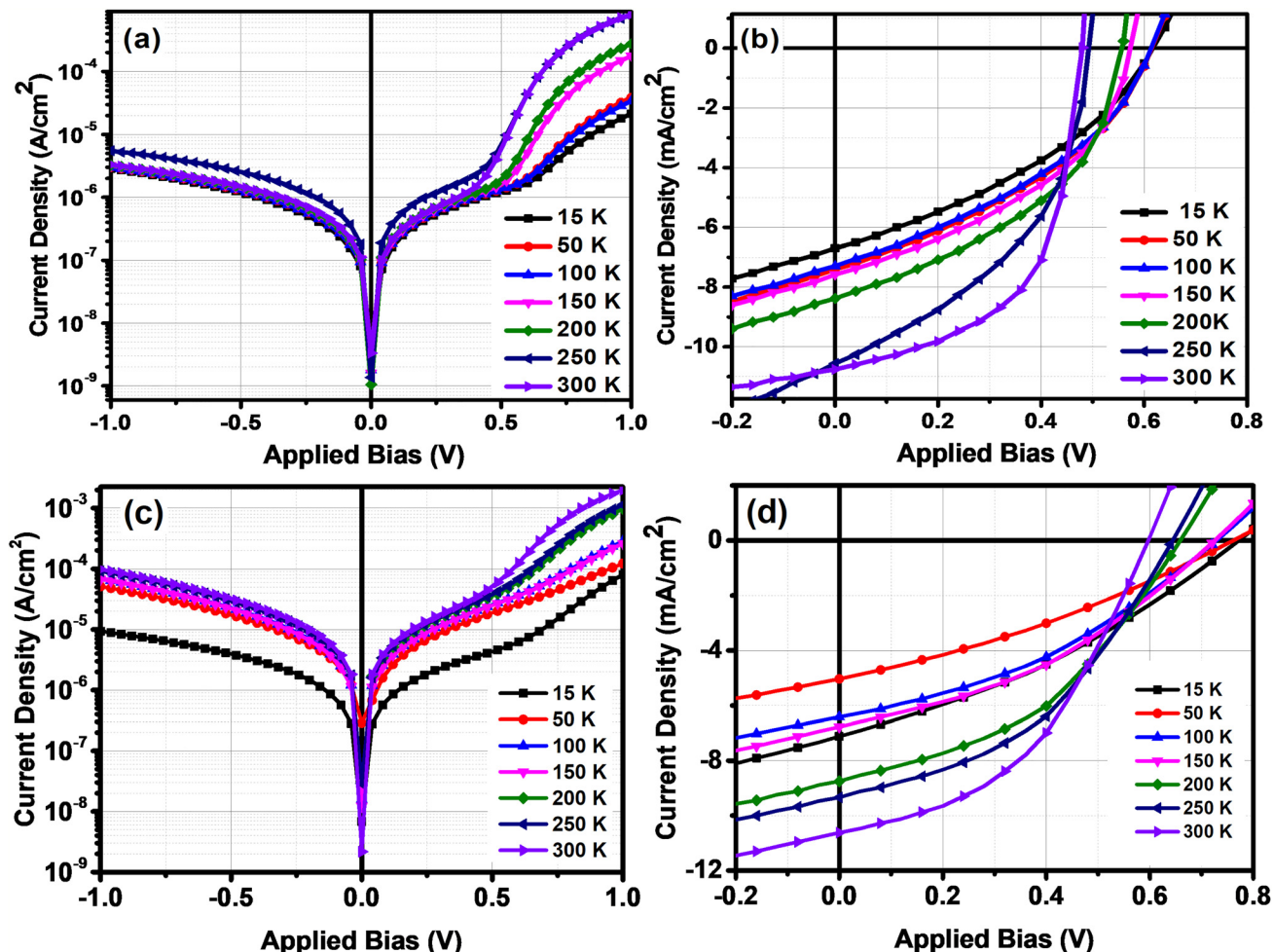


FIG. 2. (a) and (b) The current voltage characteristics under the dark and illuminated condition for the conventional structure organic solar cell. (c) and (d) The current voltage characteristics under the dark and illuminated condition for the inverted structure organic solar cell. The temperature is varied from 15 K to 300 K for each type of measurement.

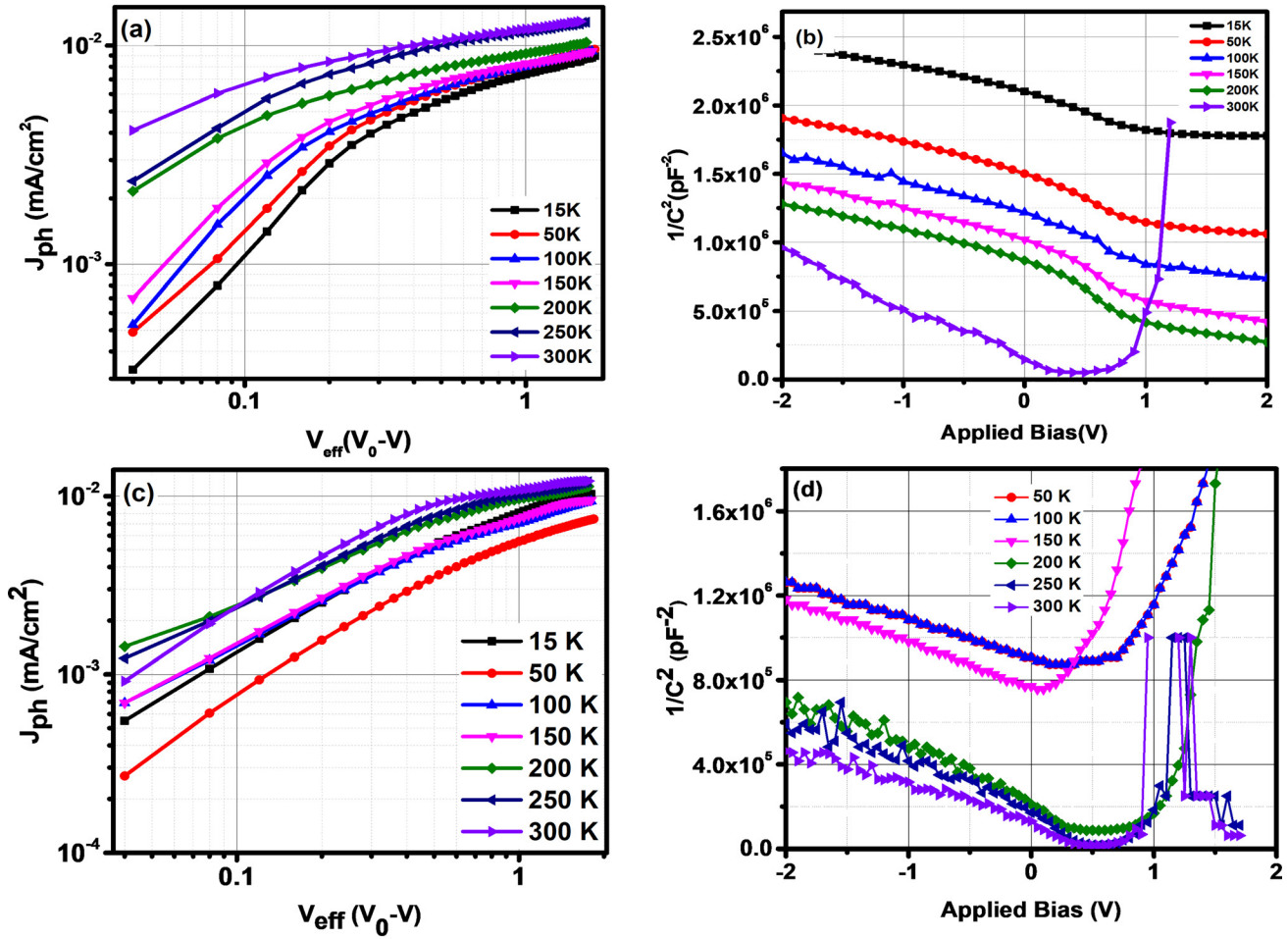


FIG. 3. The plot for photocurrent vs. effective applied bias and $1/C^2$ vs. applied bias for conventional and inverted structure organic solar cells. (a) and (b) represent the photocurrent vs. effective applied bias and $1/C^2$ vs. applied bias for conventional structure organic solar cell, respectively. (c) and (d) represent the photocurrent vs. effective applied bias and $1/C^2$ vs. applied bias for the inverted structure organic solar cell, respectively.

one sun illumination intensity using a Keithley 4200 semiconductor analyzer. A solar simulator AM1.5G (Class AAA, Photo Emission Tech.) was used for the illumination purpose. Impedance spectroscopy measurements were performed by an Autolab PGSTAT302N in the range of 100 Hz to 1 MHz. The capacitance-voltage (C-V) and capacitance frequency (C-F) measurements were performed using an Agilent 4192 A impedance analyzer in the parallel RC-circuit mode. They were recorded at a frequency of 131 kHz for extracting the V_{bi} . The AC oscillating amplitudes were selected as low as 40 mV (rms) to maintain the linearity in the response. For the low temperature measurement, samples were transferred into the vacuum chamber connected with closed cycle refrigerator systems supplied by Janis Company, and the cooling of organic solar cell devices was achieved by providing the high-pressure helium gas to the cold head with compressor.

LOW TEMPERATURE CURRENT-VOLTAGE (J-V) AND CAPACITANCE-VOLTAGE (C-V) MEASUREMENT

Figures 1(a) and 1(b) show the physical construction of conventional and inverted organic solar cells. The structural arrangement of conventional and inverted organic solar cells is ITO/MoO₃/P3HT:PC[60]BM/LiF/Al and ITO/ZnO/P3HT:PC

[60]BM/MoO₃/Ag subsequently. The active layer for both types of structures is P3HT:PC[60]BM. In the conventional structure the MoO₃ and LiF act as the hole transport layer (HTL) and electron transport layer (ETL), whereas in the inverted structure ZnO acts as the ETL and MoO₃ acts as the HTL.^{19,20} Mainly the extraction of holes and electrons is done on the exactly opposite electrode in an inverted structure compared to the conventional structure. Figures 2(a)–2(d) show the DC measurement for the conventional and inverted organic solar cell with varying temperature from 15 K to 300 K. Figures 2(a) and 2(b) show current and voltage (J-V) characteristics with temperature variation under the dark and illuminated condition for the conventional structure device, whereas Figs. 2(c) and 2(d) show the dark and illuminated J-V characteristics of the inverted structure device. The reduction in the temperature under dark conditions leads to the decrease in the reverse saturation current (J_0) for both types of devices. However, the inverted structure device shows an almost three times more decrease in the J_0 below 200 K in comparison to the conventional device. The variation in the open circuit voltage (V_{oc}) and short-circuit current (J_{sc}) is observed for conventional and inverted devices under the illuminated condition. With the decrease in the temperature, J_{sc} decreases, and an increase in the V_{oc} is observed for both types of devices. It is seen that V_{oc} tends to saturate after 100 K, and this kind of trend

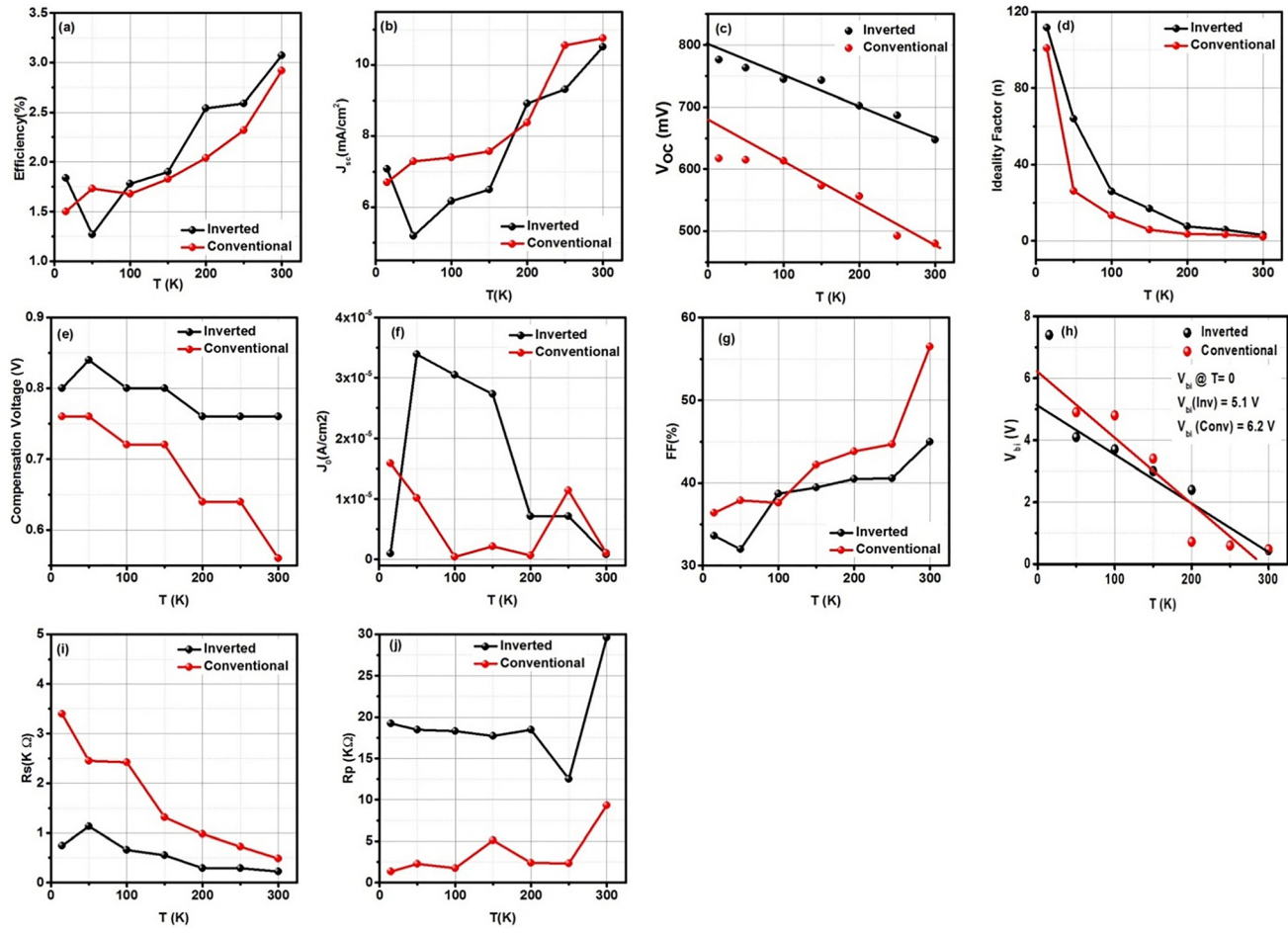


FIG. 4. The parameters extracted from Figs. 1 and 2 for the conventional and inverted structure organic solar cells as well as their variation with the temperature. Sequentially (a) efficiency vs. temperature, (b) short circuit current (J_{sc}) vs. temperature, (c) open circuit voltage (V_{oc}) vs. temperature, (d) ideality factor vs. temperature, (e) compensation voltage (V_0) vs. temperature, (f) reverse saturation current (J_0) vs. temperature, (g) fill factor (FF) vs. temperature, (h) built-in potential (V_{bi}) vs. temperature, (i) series resistance (R_s) vs. temperature and (j) shunt resistance vs. temperature.

was also observed by Jin *et al.* and attributed to lower carrier mobility at low temperature.²¹ Figures 3(a) and 3(b) show the photocurrent (J_{ph}) vs. effective applied bias plot and capacitance-voltage ($1/C^2-V$) plot for the conventional device, whereas Figs. 3(c) and 3(d) show the photocurrent vs. effective applied bias plot and capacitance-voltage ($1/C^2-V$) plot for the inverted device with varying temperature. The dark current density (J_D) is subtracted from illuminated current density (J_L) in order to find the experimental photocurrent density (J_{ph}) in the device as given in Eq. (1)²²

$$J_{ph} = J_L - J_D. \quad (1)$$

The effective bias (V_{eff}) is calculated from the subtraction of applied bias voltage from the compensation voltage (V_0)^{23,24} where compensation voltage is the voltage at which the light current is equal to the dark current, i.e., $J_{light} = J_{dark}$. At the low effective bias, diffusion current dominates, while at high effective bias ($V_{eff} > 1$ V) drift current dominates.²⁵ The significant change in the diffusion dominated photocurrent is observed with the decrease in the temperature, whereas drift dominated photocurrent remains the same in the inverted device compared to the conventional device. It shows that the carrier extraction in the inverted device is better than that in the conventional device. The Mott-Schottky plot ($1/C^2-V$)

is used to calculate built-in potential (V_{bi}) at different temperatures for the conventional and inverted device.²⁶

The comparison of the different electrical parameters with respect to the temperature has been depicted in Fig. 4. According to Table I, operating parameters are extracted from Figs. 1 and 2 for the conventional and inverted structure organic solar cells and consequently the Shockley diode equation is given in Eq. (2). The mathematical expression for the output terminal current density (J) is given as

$$J = \frac{R_{sh}}{R_s + R_{sh}} \left[J_0 e^{\left\{ \frac{q}{nkT} (V - JR_s) \right\}} - J_0 \right] + \frac{V}{R_{sh}} + J_{sc}, \quad (2)$$

where q , k , and T stand for an electronic charge, Boltzmann's constant, and operating temperature of the organic solar cell.²⁷ Figure 4(a) shows that the initially achieved efficiency at 300 K for the convention device is 2.92%, whereas for the inverted device efficiency is 3.07%. A better efficiency for the inverted device is maintained with the decrease in temperature because of the higher V_{oc} compared to the conventional device as depicted in Fig. 4(c). The J_{sc} does not perform systematically like V_{oc} as shown in Fig. 4(b). Since the same P3HT:PC[60]BM active layer is used in both types of devices, therefore opposite behaviour

TABLE I. Photovoltaic and operating parameters extracted from Figs. 1 and 2 for the conventional and inverted structure organic solar cells consequently. The effective cell area for each type of device structure is 0.09 cm^2 .

	15 K	50 K	100 K	150 K	200 K	250 K	300 K
Conventional structure organic solar cell							
Eff (%)	1.50	1.73	1.68	1.83	2.04	2.32	2.92
FF (%)	36.40	37.90	37.60	42.20	43.80	44.70	56.5
V_{oc} (mV)	617	614.6	613.6	573.1	556.6	492.3	479.9
J_{sc} (mA/cm^2)	6.7	7.4	7.29	7.58	8.38	10.56	10.76
n (IF)	100.93	26.09	13.41	5.93	3.69	3.4	2.11
J_0 (A/cm^2)	1.59×10^{-5}	1.02×10^{-5}	3.67×10^{-7}	2.15×10^{-6}	6.54×10^{-7}	1.14×10^{-5}	1.06×10^{-5}
R_s (Ω)	3398	2450	2419	1315	978	725	486
R_{sh} (Ω)	1396	2247	728	5085	2402	2305	9302
V_0 (V)	0.76	0.76	0.72	0.72	0.64	0.64	0.56
Inverted structure organic solar cell							
Eff (%)	1.84	1.27	1.78	1.90	2.54	2.59	3.07
FF (%)	33.6	32	38.7	39.5	40.5	40.6	45
V_{oc} (mV)	776.2	762.9	744.4	742.8	702.3	686.4	647.3
J_{sc} (mA/cm^2)	7.08	5.19	6.17	6.49	8.92	9.31	10.52
n (IF)	111.59	64.07	25.87	16.96	7.62	5.93	3.17
J_0 (A/cm^2)	9.45×10^{-7}	3.39×10^{-5}	3.05×10^{-5}	2.73×10^{-5}	7.14×10^{-5}	7.16×10^{-6}	7.92×10^{-7}
R_s (Ω)	740	1134	661	547	288	289	220
R_{sh} (Ω)	1.92×10^4	1.85×10^4	1.83×10^4	1.77×10^4	1.85×10^4	1.25×10^4	2.96×10^4
V_0 (V)	0.8	0.84	0.80	0.80	0.76	0.76	0.76

of V_{oc} should somehow relate to the change in the layer deposition order.¹⁷

The V_{oc} at 300 K for the conventional and inverted device is 480, and 647 mV, respectively, which further increases until 100 K and tend to saturate as shown in Fig. 4(c). By extrapolating the V_{oc} to 0 K we can find possible quasi-Fermi level separation achievable where the thermally generated electron-hole pair is fully avoided. Here, qV_{oc} at 0 K for the conventional and inverted device is 0.681 eV and 0.801 eV. Thus, the quasi-Fermi separation is larger in the case of an inverted device which leads to a better V_{oc} compared to the conventional device. The exponential decrease in ideality factor (n) until 200 K is observed for both conventional and inverted devices shown in Fig. 4(c). Figures 4(e)–4(g) show the variation in compensation voltage (V_0), reverse saturation current, and fill factor (FF) of the conventional and inverted device. The V_{bi} beyond 200 K rises very sharply for both conventional and inverted devices and linear fit shows that at 0 K it becomes 6.2 and 1 V shown in Fig. 4(h). The previous report states that very large n and V_{bi} above 200 K could be caused by R_s because at low temperature R_s becomes larger and larger which is comparable to R_{sh} as shown in Figs. 4(i) and 4(j). Hence, the Shockley diode equation cannot be simplified into the form of Eq. (2) as more voltage drop on R_s .²⁰ The reduction in the series resistance in the inverted organic solar cell is observed due to the reduced interfacial recombination loss.¹⁶

LOW TEMPERATURE IMPEDANCE SPECTROSCOPY

Furthermore, impedance measurements with respect to the temperature at different bias under the dark and illuminated conditions are performed to gain the information about the recombination in the device.²¹ The Nyquist plots are provided in Figs. 5(a)–5(d) under dark conditions at biasing voltage from 0.0 V to 0.6 V with the difference of 0.2 V, whereas

Figs. 5(e) and 5(d) are given for 0.0 V and 0.6 V under illuminated conditions. The two parallel combinations of resistance and constant phase element ($R||CPE$) connected in series together with another resistance R in series ($R-R_t||CPE_t-R_B||CPE_B$) have been used to represent the true AC behavior of charge carrier dynamics under dark and illuminated conditions.²⁸ The first parallel combination of $R_t||CPE_t$ represents contact as well as transport properties in the device, and it symbolizes the high frequency region in the Nyquist plot. The bulk property of the device is represented by the $R_B||CPE_B$ combination in the equivalent circuit where R_B represents the bulk resistance of the device and the capacitance evaluated from CPE_B commonly called chemical capacitance (C_B) originated from the polarization and accumulation of charge carriers generated at the donor-acceptor interface. Here, we observe that the bulk resistance (R_B) of the device increases due to the deprivation of thermally generated carriers but decreases with the applied bias due to the injected carriers from the electrode. Under the illuminated condition, a large decrease in R_B is recorded due to the photogenerated carriers, but at the low temperature again R_B increases due to the high recombination which reduces the J_{sc} of the device. Figure 6 shows the Bode plot for a conventional device with varying temperature at different bias under dark and illuminated conditions. The phase angle decreases and shifts towards the higher frequency with respect to the rise in temperature and it gets widened as the biasing voltage increases under the dark condition particularly. It may be caused by the less number of carriers available at low temperature. Under the illuminated condition, the phase angle shifts towards higher frequency, and it is not prominent as compared to the dark condition under low biasing situation due to the generation of photocarriers. It is observed that the inverted structured device produces high R_B compared to the conventional device due to the presence of a zinc oxide (ZnO) layer. However, under the

illuminated condition, the bulk resistance is small in the inverted structure as compared to the conventional device due to the better charge separation at the donor-acceptor interface, and flat band voltage is large due to the presence of ZnO near to the ITO (Fig. 7). The interesting difference is observed in the Bode plot of the inverted device depicted in Figs. 8(a)–8(f). Here under the dark condition and at 0.0 V biasing, the phase angle remains constant and does not shift towards high frequency with respect to the varying temperature rather remains wider compared to the conventional device. As the bias is increased up to 0.6 V change in the phase angle starts to appear, and it shifts towards a higher frequency. It shows the stability of the device with respect to the temperature but does not explain the high V_{oc} in the inverted device. Under the illuminated condition, the variation in the phase angle is completely diminished at 0.0 V bias. In the equilibrium condition, the Fermi level is aligned

across the device to the electrodes. The physical and chemical interaction between the electrodes and material results in the formation of electronic states whereas at the metal-semiconductor interface, electronic charge transfer and occupation of interfacial states produce complicated dipole moments and band bending. The work function of P3HT is close to that of the anode. Therefore, the band bending is supposed to be negligible at the MoO_3 interface in both conventional and inverted devices shown in Fig. 9. At the cathode side, the work function offset between the P3HT:PC[60]BM and LiF/Al in the conventional device and ITO/ZnO in the inverted device is compensated by the interface state induced dipole moment and band bending within the active layer to realize the Fermi-level alignment

$$qV_{oc} = E_{Fn} - E_{Fp}, \quad (3)$$

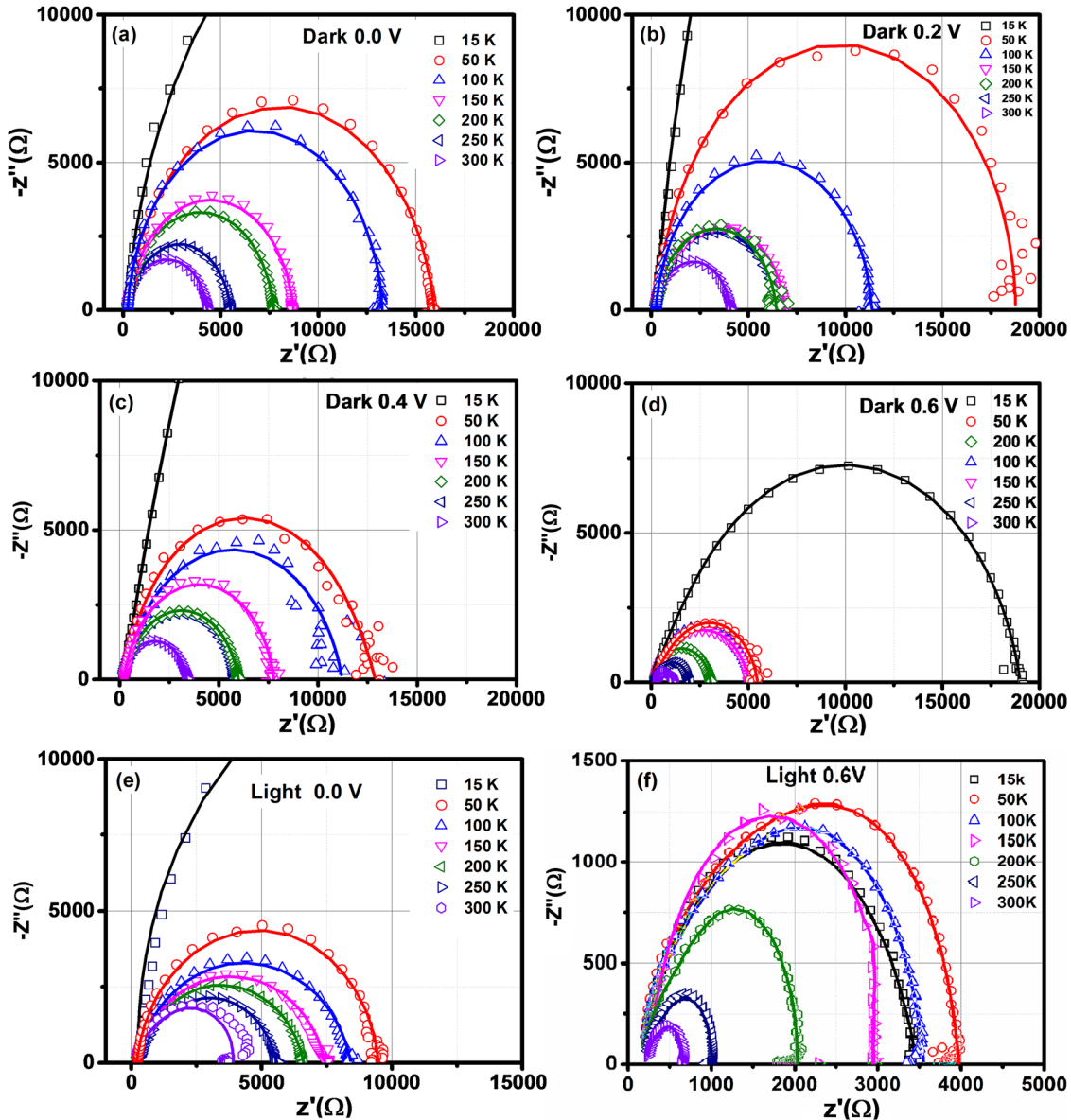


FIG. 5. Nyquist plot at different forward biasing for the conventional structure organic solar cell with varying temperature from 15 K to 300 K under dark and illuminated conditions. (a) Bias 0.0 V under dark conditions, (b) bias 0.2 V under dark conditions, (c) bias 0.4 V under dark conditions, (d) bias 0.6 V under dark conditions, (e) bias 0.0 V under illuminated conditions, and (f) bias 0.6 V under illuminated conditions. The symbols and continuous line show the experimental data and fitted data subsequently.

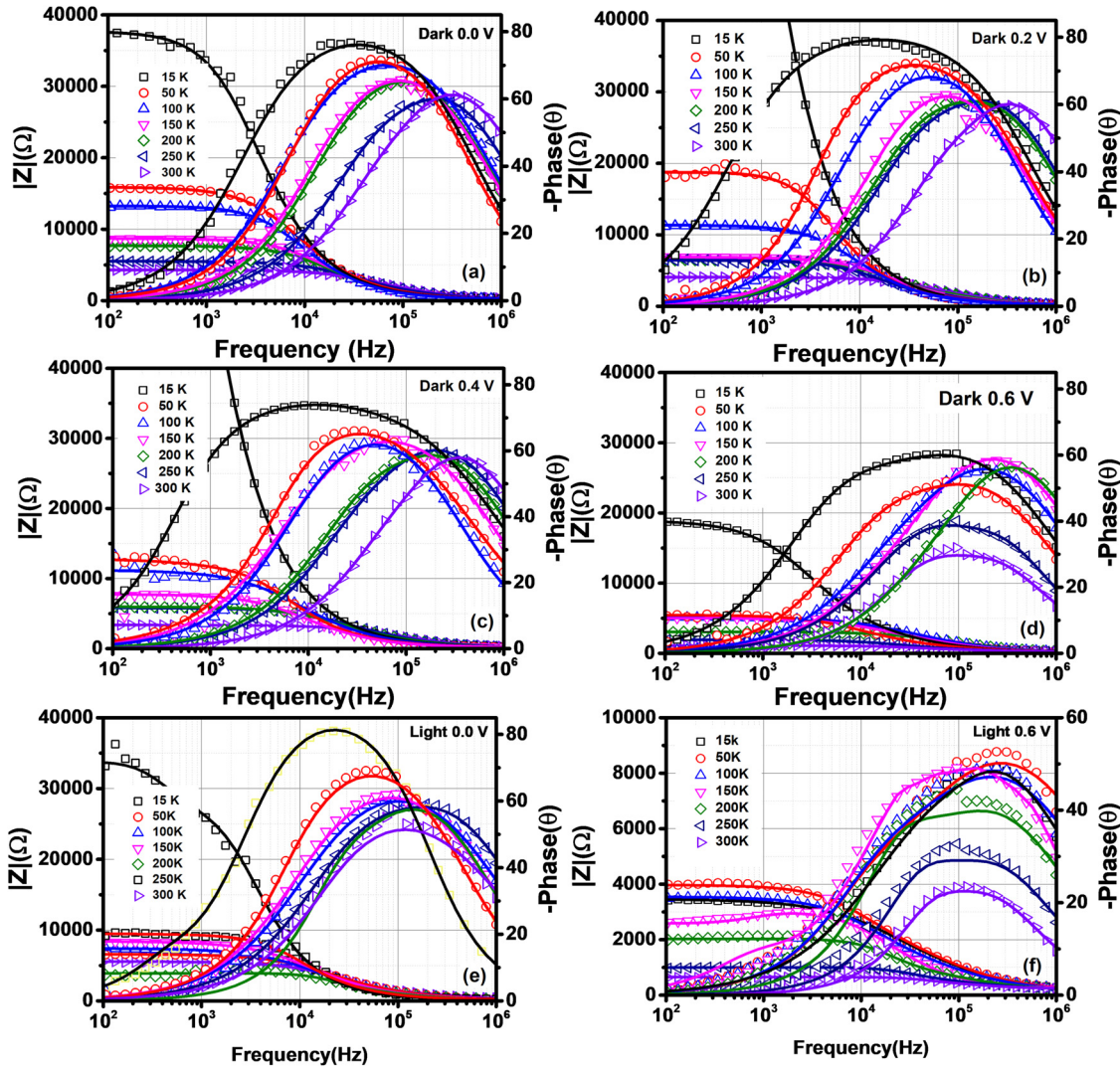


FIG. 6. Bode plot at different forward biasing for the conventional structure organic solar cell with varying temperature from 15 K to 300 K under dark and illuminated conditions. (a) Bias 0.0 V under dark conditions, (b) bias 0.2 V under dark conditions, (c) bias 0.4 V under dark conditions, (d) bias 0.6 V under dark conditions, (e) bias 0.0 V under illuminated conditions, and (f) bias 0.6 V under illuminated conditions. The symbols and continuous line show the experimental data and fitted data subsequently.

where q is the elementary charge. In this case, the upper limit of V_{oc} in devices is the energy difference of the donor (highest occupied molecular orbital) E_{HOMO} , and the acceptor lowest unoccupied molecular orbital, E_{LUMO} . Subsequently, at these energy levels, the density of states is very high, and no further split of Fermi levels is possible. Therefore, we can obtain $V_{oc} = E_g/q$, where $E_g = E_{HOMO} - E_{LUMO}$, which can be assumed as the effective bandgap of the active layer blend. However, such a limit is not reached in practical; therefore, an average downshift of 0.3 eV is observed in V_{oc} . Boix *et al.* have explained the enhanced V_{oc} in the inverted device compared to the conventional device by calculating flat band voltage (V_{fb}).¹⁷ They observed that the inverted device exhibits high V_{fb} compared to the conventional device by 30–40 mV and also the density of dopants is 6 times higher in the case of the inverted structure. Such a difference in doping levels implies that the hole quasi-Fermi level approaches the polymer HOMO by the amount equal to the $k_B T \left(\frac{N_i}{N_c} \right)$ where N_i and N_c are the doping density in inverted and conventional devices.

DEFECT DENSITY OF STATES

The energetic shift of the hole quasi-Fermi level will induce the change in the deep defect density of states near to the HOMO. Here, we have performed the capacitance frequency (CF) experiment at a different temperature to estimate the deep defect density of states. In the CF measurement, a small AC signal is applied to measure the junction capacitance, while DC bias maintains the depletion width and band bending at the metal-semiconductor interface. The available traps in the semiconductor can charge or discharge according to the applied AC signal if the energy of trap energy crosses the Fermi level. The amount of band bending provides the position of traps when the trap energy brought to the Fermi level by applying the DC bias. The applied AC signal determines the charging and discharging of the trap states.

The dependence on the AC signal comes from the thermal emission rate of traps. For the p-type semiconductor, the thermal emission rate is given as

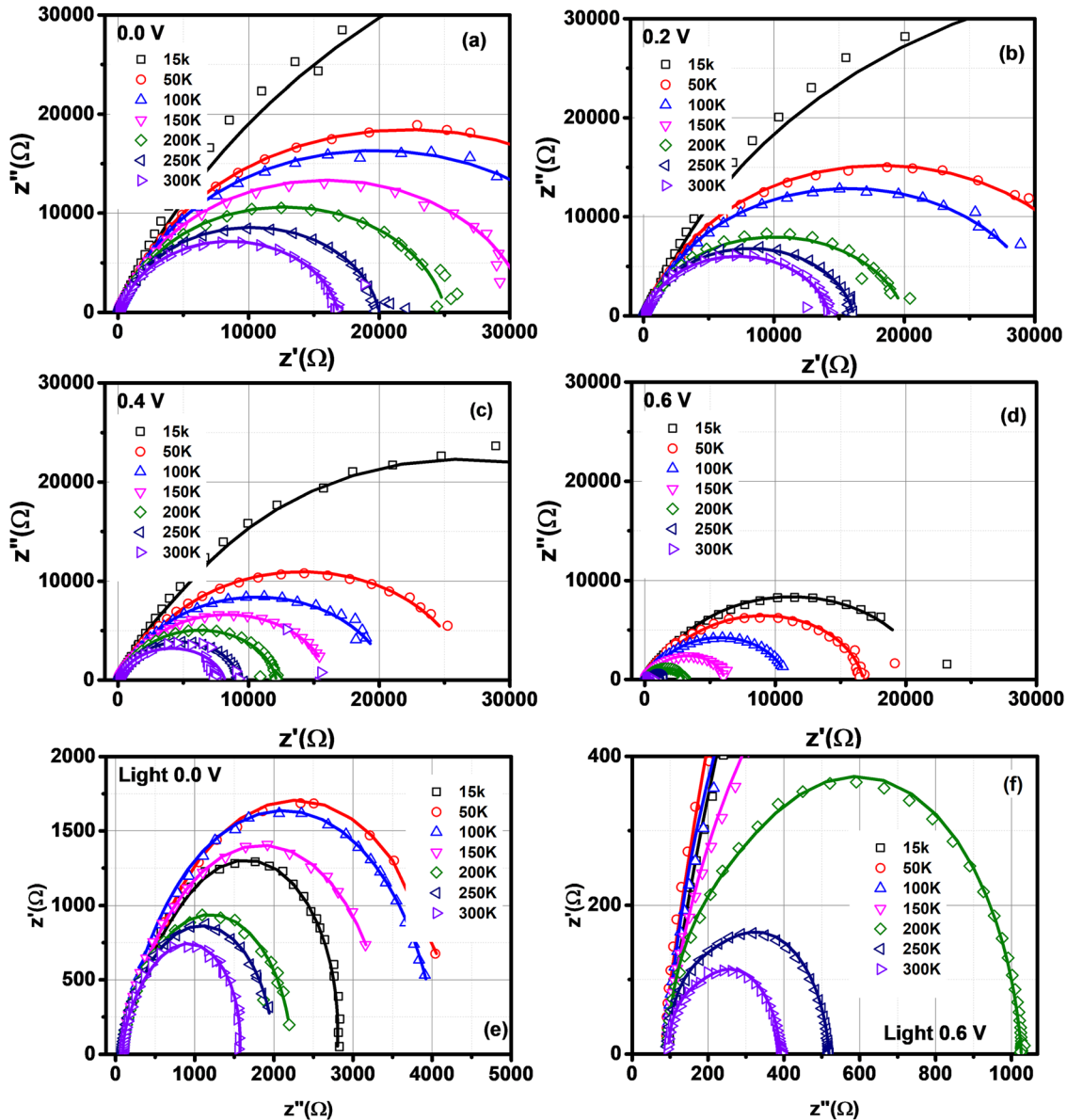


FIG. 7. Nyquist plot at different forward biasing for the inverted structure organic solar cell with varying temperature from 15 K to 300 K under dark and illuminated conditions. (a) Bias 0.0 V under dark conditions, (b) bias 0.2 V under dark conditions, (c) bias 0.4 V under dark conditions, (d) bias 0.6 V under dark conditions, (e) bias 0.0 V under illuminated conditions, and (f) bias 0.6 V under illuminated conditions. The symbols and continuous line show the experimental data and fitted data subsequently.

$$\frac{1}{\tau_p} = e_p = N_V v_{th} \sigma_p \exp^{-E_a/k_B T}, \quad (4)$$

where N_V is the effective density of states in valance band, v_{th} is thermal velocity, σ_p is the capture cross section, E_a is the trap activation energy, K_B is the Boltzmann constant, and T is temperature in Kelvin.^{29,30} In the case of the organic semiconductor $N_V v_{th} \sigma_p$ is assumed to be temperature independent³¹ and named attempt to escape frequency.³² The attempt to escape frequency (v_0) can determine the maximum trap emission rate. By linearizing the following equation:

$$\ln(e_p) = \frac{-E_a}{K_B T} + \ln(v_0), \quad (5)$$

where $v_0 = N_V v_{th} \sigma_p = \frac{\omega_0}{2\pi}$, an Arrhenius plot of $\ln(e_p)$ with $1000/T$ appears as a straight line and the slope of the straight line gives the trap activation energy (E_a) and intercept

provide the v_0 . The attempt to escape frequency and frequency of the applied AC signal can determine the demarcation energy which is given by the following equation derived by Walter *et al.*:³³

$$E_\omega = K_B T \ln\left(\frac{\omega_0}{\omega}\right). \quad (6)$$

Here, ω is the frequency of the applied AC signal. The traps cannot respond if the demarcation energy is below the hole quasi-Fermi level (E_{FP}). Using this concept, the trap state above the hole quasi-Fermi level can be detected. The defect density distribution above the hole quasi-Fermi level and above the HOMO of the organic semiconductor can be determined by taking the derivative of the CF profile as

$$N_t(E_\omega) = -\frac{V_{bi}}{qW} \frac{dC}{d\omega} \frac{\omega}{K_B T}, \quad (7)$$

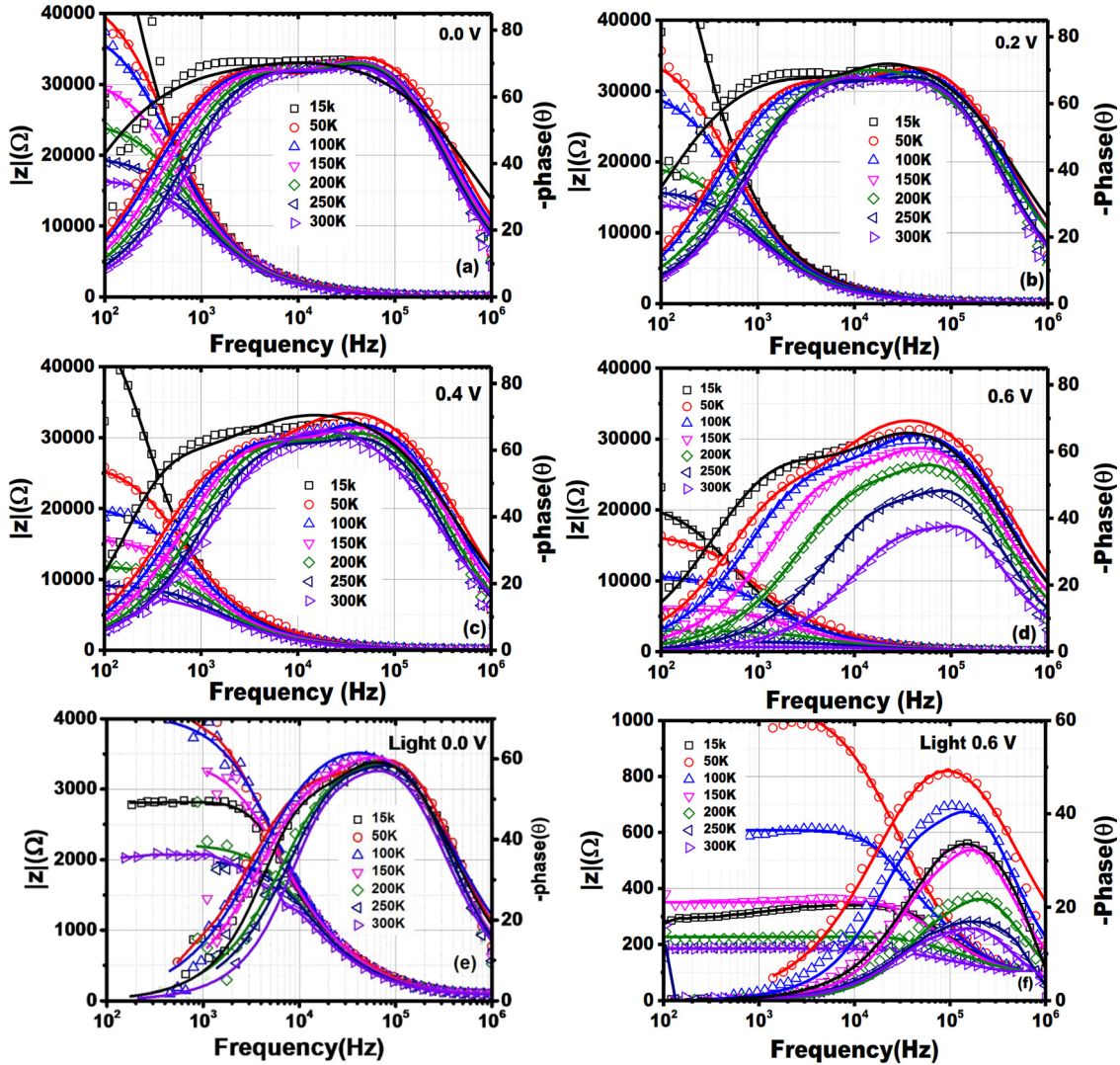


FIG. 8. Bode plot at different forward biasing for the inverted structure organic solar cell with varying temperature from 15 K to 300 K under dark and illuminated conditions. (a) Bias 0.0 V under dark conditions, (b) bias 0.2 V under dark conditions, (c) bias 0.4 V under dark conditions, (d) bias 0.6 V under dark conditions, (e) bias 0.0 V under illuminated conditions, and (f) bias 0.6 V under illuminated conditions. The symbols and continuous line show the experimental data and fitted data subsequently to the respective temperature.

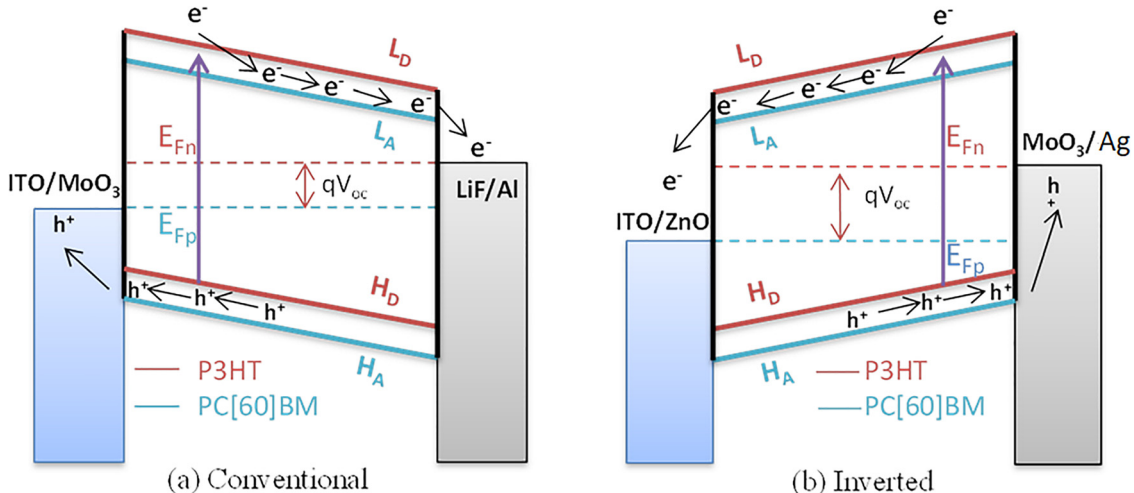


FIG. 9. The separated quasi-Fermi levels of electron and holes under the illuminated condition for (a) conventional organic solar cell (ITO/MoO₃/P3HT:PC[60]BM/LiF/Al) and (b) inverted organic solar cell (ITO/ZnO/P3HT:PC[60]BM/MoO₃/Ag). HD and LD depict the donor's HOMO LUMO whereas HA and LA depict the acceptor's HOMO LUMO.

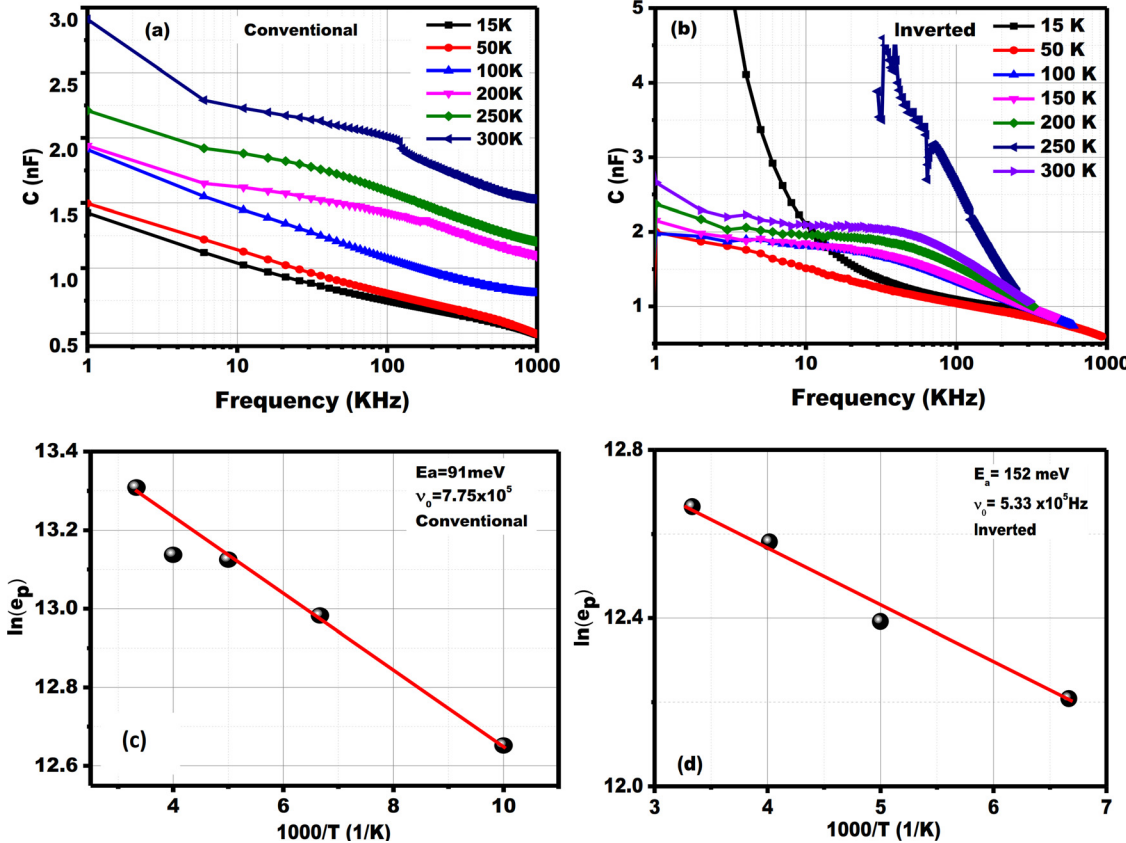


FIG. 10. (a) Capacitance frequency plot for the conventional structure organic solar cell under dark conditions. (b) Capacitance frequency plot for the inverted structure organic solar cell under dark conditions. (c) Arrhenius plot for the conventional structure organic solar cell. (d) Arrhenius plot for the inverted structure organic solar cell. The inset of figure (c) and (d) shows the evaluated activation energy and escape frequency for conventional and inverted structure organic solar cells, respectively.

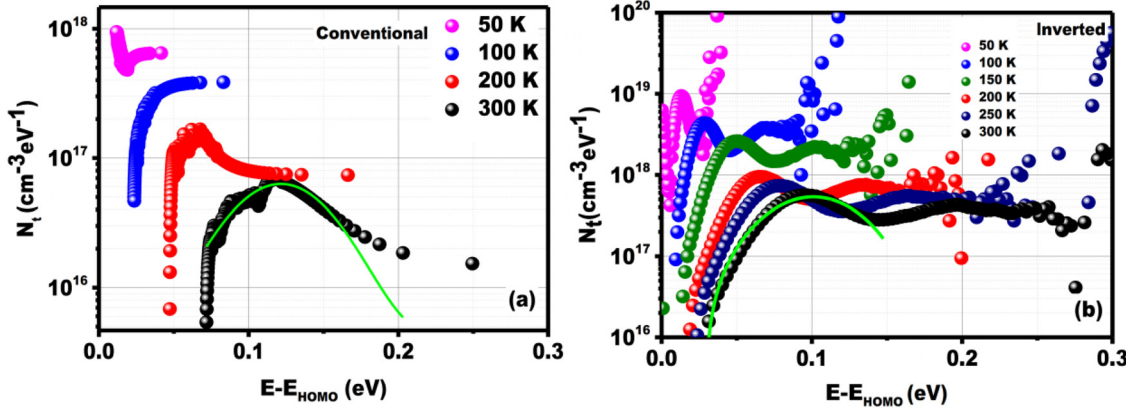


FIG. 11. Defect density profile for the derived (a) conventional structure organic solar cell and (b) inverted structure organic solar cell.

where C and W are the capacitance and depletion width of the junction consequently. The built-in potential (V_{bi}) at the junction is calculated by the capacitance-voltage (CV) measurement by utilizing the Mott-Schottky (M-S) relation given in Eq. (8)

$$\frac{1}{C^2} = \frac{2}{A^2 q \epsilon N_A} (V_{bi} - V_{dc}). \quad (8)$$

Here, V_{dc} is applied bias, N_A is doping concentration in the organic semiconductor, ϵ is the dielectric constant, and A is an area of the device. $1/C^2$ vs. V_{dc} slope gives the doping concentration and V_{bi} .

Figures 10(a) and 10(b) show the CF measurement for the conventional and inverted device at a different temperature. The frequency at which abrupt change in capacitance takes place describes the demarcation energy (E_ω) where the traps respond. Then, the peak in the $f\partial C/\partial f$ plot with frequency identifies the frequency step which coincides with the emission rate (e_p). The linear fit of $\ln(e_p)$ vs. $1000/T$ plot given in Figs. 10(c) and 10(d) provides the activation energy and attempt to escape frequency which is later used in the calculation of demarcation energy and defect density of states for the conventional and inverted device. Some points in the Arrhenius plot are intentionally avoided due to

TABLE II. Calculated peak position and the width of the distribution of defects from the Gaussian distribution for the conventional, inverted device based on P3HT:PC[60]BM and PCE10:PC[70]BM inverted device according to Eq. (9).

Device structure	E_0 (eV)	σ (meV)	h ($\text{cm}^{-3}\text{eV}^{-1}$)	N_t (cm^{-3})
Conventional	0.12	75.0	7.0×10^{16}	4.4×10^{16}
Inverted	0.10	33.1	5.7×10^{17}	4.9×10^{16}

generated noise during the differentiation of CF ($\text{d}F/\text{d}C$). The calculated activation energy (E_a) and an attempt to escape frequency for the conventional device are 91 meV and 7.75×10^5 Hz, whereas for the inverted device are 152 meV and 5.33×10^5 Hz. By utilizing Eq. (7), the calculated deep defect density of states for the conventional and inverted device has been plotted against the demarcation energy to analyze the energetic disorder distribution as given in Figs. 11(a) and 11(b). Both of the devices show Gaussian distribution which was confirmed by the Gaussian fit at 300 K using the following equation:³⁴

$$N_t(E_0) = \frac{N_t}{\sqrt{2\pi\sigma}} \exp\left[\frac{-(E_0 - E_0)^2}{2\sigma^2}\right], \quad (9)$$

where N_t , E_0 , and σ are the defect density, mean energy of the defect distribution, and disorder parameter subsequently. The parameters evaluated after the fitting of Eq. (7) have been organized in Table II. The important observation from the defect density of states profile is that the center of Gaussian distribution is shifted to high energy as the temperature is increased which is an indication of the creation of shallow traps in polymers. At very low temperature (< 100 K), distribution of defect states is very small and shifts near to the HOMO of polymers. The increase in the open circuit voltage at low temperature can also be related to the decrease in the deep defect states.

The mean energy of the defect distribution for all devices is around 0.1 eV. The doping concentration is directly related to the disorder parameter, σ (half of the width of the distribution). The electronic sites are localized hopping sites in the disordered organic semiconductor. The charge species in an organic semiconductor get affected by the Coulombic interaction due to a low dielectric constant. The disorder in the organic semiconductor produces a random distribution of free carriers which can interact with the carriers localized at the hopping sites. Therefore, the broadening of tail states in the deep defect state is observed. In the inverted device, the disorder parameter is 33 meV, whereas in the conventional device it becomes 75 meV. This implies that the energetic disorder is reduced in an inverted device which helps to increase open circuit voltage. The height of Gaussian distribution (h) and defect density (N_t) are high in the case of an inverted device that could be possible because of the interface of ZnO and Ag which can be further reduced by replacing Ag to Au and with optimization of the ZnO layer.

CONCLUSION

In conclusion, the exploration of conventional and inverted organic solar cells reveals that the increased open

circuit voltage in the inverted device is due to creation of less energetic disorder into the bandgap of the photoactive layer in comparison to the conventional device. The enhancement in open circuit voltage at low temperature is also observed which is described by the shifting of hole and electron quasi-Fermi levels of the donor-acceptor material. The important observation from the defect density of states profile is that the center of Gaussian distribution is shifted to high energy as the temperature is increased which is an indication of the creation of shallow traps in polymers. In the inverted device, the disorder parameter (σ) is 33 meV, whereas in the conventional device it becomes 75 meV. This suggests that the energetic disorder is reduced in an inverted device due to which improvement in open circuit voltage is observed.

ACKNOWLEDGMENTS

The authors are thankful to the Director, National Physical Laboratory, Dr. K. S. Krishnan Marg, New Delhi, for his kind support. The authors gratefully recognize the financial support from the project. A.R. is thankful to University Grant Commission, New Delhi, India, for the award of Senior Research Fellowship. One of the authors S.C., who has been the India coordinator for the Indo-UK project entitled “Advancing the Production Potential and Efficiency of Excitonic solar cells (APEX),” is thankful to DST for funding this program.

- ¹P. J. Jadhav, P. R. Brown, N. Thompson, B. Wunsch, A. Mohanty, S. R. Yost, E. Hontz, T. Van Voorhis, M. G. Bawendi, V. Buloviä, and M. A. Baldo, *Adv. Mater.* **24**, 6169 (2012).
- ²D. H. Wang, D. Y. Kim, K. W. Choi, J. H. Seo, S. H. Im, J. H. Park, O. O. Park, and A. J. Heeger, *Angew. Chem. (Int. Ed. English)* **50**, 5519 (2011).
- ³R. C. I. MacKenzie, C. G. Shuttle, G. F. Dibb, N. Treat, E. von Hauff, M. J. Robb, C. J. Hawker, M. L. Chabinyc, and J. Nelson, *J. Phys. Chem. C* **117**, 12407 (2013).
- ⁴K. S. Nalwa, H. K. Kodali, B. Ganapathysubramanian, and S. Chaudhary, *Appl. Phys. Lett.* **99**, 263301 (2011).
- ⁵C. M. Proctor, M. Kuik, and T.-Q. Nguyen, *Prog. Polym. Sci.* **38**, 1941–1960 (2013).
- ⁶J. Nelson, S. A. Choulis, and J. R. Durrant, *Thin Solid Films* **451–452**, 508 (2004).
- ⁷G. Garcia-Belmonte and J. Bisquert, *Appl. Phys. Lett.* **96**, 113301 (2010).
- ⁸S. D. Collins, C. M. Proctor, N. A. Ran, and T.-Q. Nguyen, *Adv. Energy Mater.* **6**, 1501721 (2016).
- ⁹J. C. Blakesley and D. Neher, *Phys. Rev. B* **84**, 075210 (2011).
- ¹⁰N. K. Elumalai and A. Uddin, *Energy Environ. Sci.* **9**, 391 (2016).
- ¹¹M. C. Scharber, D. Mühlbacher, M. Koppe, P. Denk, C. Waldauf, A. J. Heeger, and C. J. Brabec, *Adv. Mater.* **18**, 789 (2006).
- ¹²K. Vandewal, K. Tvingstedt, A. Gadisa, O. Inganäs, and J. V. Manca, *Nat. Mater.* **8**, 904 (2009).
- ¹³C. Deibel, T. Strobel, and V. Dyakonov, *Adv. Mater.* **22**, 4097 (2010).
- ¹⁴P. P. Boix, G. Garcia-Belmonte, U. Muniecas, M. Neophytou, C. Waldauf, and R. Pacios, *Appl. Phys. Lett.* **95**, 233302 (2009).
- ¹⁵U. K. Verma, D. C. Tripathi, and Y. N. Mohapatra, *Appl. Phys. Lett.* **109**, 113301 (2016).
- ¹⁶C.-Z. Li, C.-Y. Chang, Y. Zang, H.-X. Ju, C.-C. Chueh, P.-W. Liang, N. Cho, D. S. Ginger, and A. K.-Y. Jen, *Adv. Mater.* **26**, 6262 (2014).
- ¹⁷P. P. Boix, J. Ajuria, I. Etxebarria, R. Pacios, G. Garcia-Belmonte, and J. Bisquert, *J. Phys. Chem. Lett.* **2**, 407 (2011).
- ¹⁸S. Lattante, *Electronics* **3**, 132 (2014).
- ¹⁹D. W. Zhao, S. T. Tan, L. Ke, P. Liu, A. K. K. Kyaw, X. W. Sun, G. Q. Lo, and D. L. Kwong, *Sol. Energy Mater. Sol. Cells* **94**, 985 (2010).
- ²⁰F. Liu, S. Shao, X. Guo, Y. Zhao, and Z. Xie, *Sol. Energy Mater. Sol. Cells* **94**, 842 (2010).
- ²¹M. I. Nugraha, R. Häusermann, S. Z. Bisri, H. Matsui, M. Sytnyk, W. Heiss, J. Takeya, and M. A. Loi, *Adv. Mater.* **27**, 2107 (2015); Z. Jin, A. Wang, Q. Zhou, Y. Wang, and J. Wang, *Sci. Rep.* **6**, 37106 (2016).

- ²²F. Hermerschmidt, A. Savva, E. Georgiou, S. M. Tuladhar, J. R. Durrant, I. McCulloch, D. D. C. Bradley, C. J. Brabec, J. Nelson, and S. A. Choulis, *ACS Appl. Mater. Interfaces* **9**, 14136 (2017).
- ²³J. Yu, J. Huang, L. Zhang, and Y. Jiang, *J. Appl. Phys.* **106**, 063103 (2009).
- ²⁴W. E. I. Sha, X. Li, and W. C. H. Choy, *Sci. Rep.* **4**, 6236 (2014).
- ²⁵M. B. Upama, M. Wright, B. Puthen-Veettil, N. K. Elumalai, M. A. Mahmud, D. Wang, K. H. Chan, C. Xu, F. Haque, and A. Uddin, *RSC Adv.* **6**, 103899 (2016).
- ²⁶F. Cardon and W. P. Gomes, *J. Phys. D: Appl. Phys.* **11**, L63 (1978).
- ²⁷D. Bozyigit, W. M. M. Lin, N. Yazdani, O. Yarema, and V. Wood, *Nat. Commun.* **6**, 6180 (2015).
- ²⁸P. Córdoba-Torres, T. J. Mesquita, and R. P. Nogueira, *J. Phys. Chem. C* **119**, 4136 (2015).
- ²⁹D. Abou-Ras, T. Kirchartz, and U. Rau, *Advanced Characterization Techniques for Thin Film Solar Cells* (Wiley-VCH Verlag GmbH & Co. KGaA, Weinheim, Germany, 2011).
- ³⁰L. C. Kimerling, *J. Appl. Phys.* **45**, 1839 (1974).
- ³¹J. A. Carr and S. Chaudhary, *Energy Environ. Sci.* **6**, 3414 (2013).
- ³²S. S. Hegedus and E. A. Fagen, *J. Appl. Phys.* **71**, 5941 (1992).
- ³³T. Walter, R. Herberholz, C. Müller, and H. W. Schock, *J. Appl. Phys.* **80**, 4411 (1996).
- ³⁴T. Muntasir and S. Chaudhary, *J. Appl. Phys.* **118**, 205504 (2015).